
Article:
Shaw, J. orcid.org/0000-0002-0928-3604, Kesserwani, G. and Pettersson, P. (2020) Probabilistic Godunov-type hydrodynamic modelling under multiple uncertainties: robust wavelet-based formulations. Advances in Water Resources. 103526. ISSN 0309-1708

https://doi.org/10.1016/j.advwatres.2020.103526

Probabilistic Godunov-type hydrodynamic modelling under multiple uncertainties: robust wavelet-based formulations

James Shaw[a], Georges Kesserwani[a,*], Per Pettersson[b]

[a]*Department of Civil and Structural Engineering, The University of Sheffield, Western Bank, Sheffield S10 2TN, U.K.*
[b]*NORCE Norwegian Research Centre, N-5838 Bergen, Norway*

Abstract

Intrusive stochastic Galerkin methods propagate uncertainties in a single model run, eliminating repeated sampling required by conventional Monte Carlo methods. However, an intrusive formulation has yet to be developed for probabilistic hydrodynamic modelling incorporating robust wetting-and-drying and stable friction integration under joint uncertainties in topography, roughness, and inflow. Robustness measures are well-developed in deterministic models, but rely on local, nonlinear operations that can introduce additional stochastic errors that destabilise an intrusive model. This paper formulates an intrusive hydrodynamic model using a multidimensional tensor product of Haar wavelets to capture fine-scale variations in joint probability distributions and extend the validity of robustness measures from the underlying deterministic discretisation. Probabilistic numerical tests are designed to verify intrusive model robustness, and compare accuracy and efficiency against a conventional Monte Carlo approach and two other alternatives: a nonintrusive stochastic collocation formulation sharing the same tensor product wavelet basis, and an intrusive formulation that truncates the basis to gain efficiency under multiple uncertainties. Tests reveal that: (i) a full tensor product basis is required to preserve intrusive model robustness, while the nonintrusive counterpart achieves identically accurate results at a reduced computational cost; and, (ii) Haar wavelets basis requires at least three levels of refinements per uncertainty dimension to reliably capture complex probability distributions. Accompanying model software and simulation data are openly available online.

Keywords: Probabilistic finite volume formulation; Intrusive and nonintrusive stochastic approaches; Multiscale basis functions; multidimensional uncertainty space; robust wetting-and-drying and friction treatments; accuracy, efficiency and reliability analyses.

1. Introduction

Measurement uncertainties in topographic elevation, roughness, and inflow discharge are neglected by deterministic hydrodynamic models, but these uncertainties can strongly affect water depths, flow velocities and wave arrival times in flood inundation predictions (Bates et al., 2014; Dimitriadis et al., 2016; Kim and Sanders, 2016). By propagating these input uncertainties forward into a probabilistic solution of the flow, probabilistic hydrodynamic models avoid spuriously precise predictions and prevent overconfidence in deterministic models (Beven, 2005; Di Baldassarre et al., 2010). Probabilistic

*Corresponding author
Email addresses: js102@zepler.net (James Shaw), g.kesserwani@shef.ac.uk (Georges Kesserwani), pepe@norceresearch.no (Per Pettersson)

modelling under multiple uncertainties is often computationally expensive because conventional Monte Carlo sampling requires thousands of deterministic model runs (Neal et al., 2013; Jung and Merwade, 2011; Di Baldassarre et al., 2010). This study investigates more efficient alternatives that use a wavelet-based representation of the probabilistic flow.

Alternatives to conventional Monte Carlo sampling include multilevel Monte Carlo (MLMC) methods, the cumulative distribution function (CDF) approach, and stochastic collocation and stochastic Galerkin methods. MLMC methods sample at different mesh refinement levels, with only a few samples taken on the finest meshes. Mishra et al. (2012) developed a MLMC hydrodynamic model using Haar wavelets to generate a multilevel representation of uncertain topography. In the CDF approach, the governing equations are manipulated to obtain a linear differential equation that can be solved more easily, which has been demonstrated for kinematic wave routing problems (Wang and Tartakovsky, 2012; Cheng et al., 2019).

Stochastic collocation and stochastic Galerkin methods substantially reduce or eliminate the need for repetitive sampling (Xiu, 2009), and are adopted in this study to develop robust probabilistic hydrodynamic formulations. Both methods capture the spatial and temporal evolution in probability distributions of the flow variables, with each probability distribution approximated by a low-order basis expansion using a small set of coefficients called *stochastic modes*. Global orthogonal polynomials from the Askey scheme are often chosen as basis functions because they exactly represent the most common probability distributions: for example, Hermite polynomials exactly represent any Gaussian distribution with only two stochastic modes (Xiu and Karniadakis, 2002). As a result, stochastic collocation and stochastic Galerkin methods are known collectively as polynomial chaos methods. When multiple sources of uncertainty are considered, then the probability distributions become multivariate, joint distributions that are defined on a multidimensional uncertainty space. As this dimensionality increases, the number of basis functions can grow exponentially, increasing computational and storage costs—the so-called curse of dimensionality (Xiu, 2009).

Nevertheless, compared to Monte Carlo sampling, stochastic collocation requires a relatively small set of model runs, each initialised with specific input values chosen to minimise the required number of runs (Xiu and Hesthaven, 2005). Stochastic collocation is attractive because it is a *nonintrusive* method, which can be used with any existing deterministic model. Substantial efficiency gains have been reported for nonintrusive hydrodynamic models: Ge and Cheung (2011) modelled long-wave runup processes where uncertainties in topography, roughness and input wave height were considered individually, and El Moçayd et al. (2018) studied steady-state subcritical river flow under joint uncertainties in roughness and inflow discharge. Wang et al. (2019) also incorporated a nonintrusive hydrodynamic model into a data assimilation framework in order to infer river bathymetry from observed water depths.

Unlike nonintrusive methods, stochastic Galerkin involves an *intrusive* mathematical reformulation of an existing deterministic discretisation, yielding a new intrusive model that directly evolves the probabilistic flow solution in a single model run (Xiu and Karniadakis, 2002). Some studies of probabilistic elliptic problems have found that an intrusive method can outperform a nonintrusive method (Elman et al., 2011; Son and Du, 2020), while Bäck et al. (2011) found that both methods have a similar cost for a different class of elliptic problems. Hence, the potential computational benefits are highly dependent on the particular application and model formulation, and have yet to be studied for robust hydrodynamic modelling. Intrusive hydrodynamic models have been reported to be 50–100 times faster than Monte Carlo (Ge et al., 2008;

Shaw and Kesserwani, 2020), but all tests were limited to a single source of uncertainty, and the intrusive models lacked any treatment of wetting-and-drying or frictional forces.

Robustness measures for depth positivity preservation at wet-dry fronts and stable friction integration are already well-developed for deterministic modelling (e.g. Liang and Marche, 2009; Kesserwani, 2013; Murillo and Navas-Montilla, 2016), but their extension into an intrusive hydrodynamic model remains to be explored. Robustness measures typically involve local, nonlinear operations on topography and flow variables that give rise to local, nonlinear variations in probability distributions (Shaw and Kesserwani, 2020; Abgrall and Mishra, 2017). These local, nonlinear variations are poorly represented by global polynomial basis functions, and spurious undershoots in a polynomial approximation can result in predicted negative water depths that will crash an intrusive hydrodynamic model (Shaw and Kesserwani, 2020).

The shortcomings of global polynomial basis functions has motivated alternative approaches capable of representing local, nonlinear variations in any probability distribution. Le Maître et al. (2004a) first proposed using Haar wavelets, which are multiscale, recursively nested and overlapping basis functions, to provide a localised, piecewise-constant decomposition of any probability distribution. The approach was later generalised using multiwavelets to provide a piecewise-polynomial representation (Le Maître et al., 2004b), and (multi)wavelet basis functions have been successfully applied to intrusive models of the Euler equations (Pettersson et al., 2014), and the Buckley-Leverett equation for groundwater flow (Pettersson and Tchelepi, 2016).

Under multiple sources of uncertainty, the number of wavelet basis functions required to span the multidimensional uncertainty space can grow exponentially, increasing computational and storage costs. This curse of dimensionality is commonly alleviated by exploiting the localised multiscale nature of wavelets: dynamic adaptivity can be implemented via multiresolution analysis (Le Maître et al., 2004b; Tryoen et al., 2012; Abgrall et al., 2017), or the wavelet basis can be truncated to remove basis functions representing fine-scale cross-dependencies (Le Maître et al., 2004a). Basis truncation has been proven to preserve robustness measures in the deterministic case for a discontinuous Galerkin hydrodynamic model (Kesserwani et al., 2018), but the impact of truncation has yet to be studied for probabilistic hydrodynamic modelling.

Wavelet-based stochastic methods have the potential to gain efficiency over Monte Carlo methods, while simultaneously preserving robust wetting-and-drying and friction treatments under joint uncertainties. This paper examines the potential of wavelet-based methods by formulating intrusive and nonintrusive Godunov-type hydrodynamic models to compare their accuracy, efficiency and robustness against a Monte Carlo approach. This represents a substantial advance beyond existing intrusive models that were limited to frictionless flows on fully-wet domains involving only a single source of uncertainty (Ge et al., 2008; Shaw and Kesserwani, 2020).

The remainder of this paper is organised as follows: section 2 presents a wavelet-based stochastic Galerkin reformulation of a one-dimensional finite volume Godunov-type model, and section 3 presents its nonintrusive counterpart. In section 4, the probabilistic models are validated in a series of four numerical tests: the first two tests are employed to verify the preservation of well-balancedness with wetting-and-drying and frictional effects in the intrusive model, and to study the impact of basis truncation on model robustness and stability; the final two tests measure the efficiency and reliability of the intrusive and nonintrusive models to capture water depth probability distributions under transcritical steady-state conditions. Conclusions are drawn in section 5. Numerical simulation data (Shaw et al., 2020b) and Python 3 model codes (Shaw et al.,

2020a) are available to download from Zenodo, with accompanying instructions provided in Appendix C.

2. Intrusive finite volume formulation

This section presents an intrusive modelling approach that is specifically designed to extend robustness measures from a deterministic context into a probabilistic context under multiple sources of uncertainty. Haar wavelet basis functions are adopted to span the space of multiple uncertainty dimensions, enabling the preservation of robustness measures from any deterministic finite volume hydrodynamic model into its stochastic extension via an intrusive modelling approach.

The particular intrusive finite volume formulation presented here is a stochastic extension of the deterministic one-dimensional (1D) shallow water equations written in conservative vectorial form as (Toro and Garcia-Navarro, 2007):

$$\frac{\partial \mathbf{U}}{\partial t} + \frac{\partial \mathbf{F}(\mathbf{U})}{\partial x} = \mathbf{S}_\mathrm{b} + \mathbf{S}_\mathrm{f}\,, \tag{1}$$

where $\mathbf{U}$ is the vector of flow variables, $\mathbf{F}(\mathbf{U})$ is the flux vector, and the source term vectors $\mathbf{S}_\mathrm{b}$ and $\mathbf{S}_\mathrm{f}$ represent topographic slopes and frictional effects respectively:

$$\mathbf{U} = \begin{bmatrix} h \\ q \end{bmatrix}, \mathbf{F} = \begin{bmatrix} q \\ \dfrac{q^2}{h} + \dfrac{gh^2}{2} \end{bmatrix}, \mathbf{S}_\mathrm{b} = \begin{bmatrix} 0 \\ -gh\dfrac{\mathrm{d}z}{\mathrm{d}x} \end{bmatrix}, \text{ and } \mathbf{S}_\mathrm{f} = \begin{bmatrix} 0 \\ S_\mathrm{f} \end{bmatrix}, \tag{2}$$

with water depth h [L] and unit-width discharge $q = hu$ [L^2/T] in which u is the depth-averaged horizontal velocity [L/T]. The topography profile is $z(x)$ [L], and g is the gravitational acceleration [$\mathrm{L/T}^2$].The friction source term is $S_\mathrm{f} = -C_\mathrm{f} u\,|u|$ where the roughness coefficient is $C_\mathrm{f} = g n_\mathrm{M}^2 / h^{1/3}$ and n_M is the Manning's parameter [$\mathrm{T/L}^{1/3}$].

A finite volume discretisation of Eq. (1) is adopted where the discrete flow vector $\mathbf{U}_i^n$ and topography z_i at a physical element i and time level n are represented as piecewise-constant fields over a uniform 1D mesh with physical elements of size Δx.

2.1. Initialisation of uncertain inputs

Uncertain inputs are identified for a given scenario, which can include the Manning's parameter, topography profile, boundary conditions and initial conditions, and each input is initialised with a prescribed probability distribution. Given D mutually independent and uncorrelated uncertain inputs, each input is assigned to an uncertainty dimension $\xi_1, \ldots, \xi_D$, forming a D-dimensional uncertainty space $\boldsymbol{\xi} \in [-1, 1]^D$. An uncertainty space is introduced into every variable $A(\boldsymbol{\xi}) \in \{h_i^n(\boldsymbol{\xi}), q_i^n(\boldsymbol{\xi}), z_i(\boldsymbol{\xi}), n_\mathrm{M}(\boldsymbol{\xi})\}$, such that each deterministic variable becomes a stochastic variable that is expressed as a basis expansion:

$$A(\boldsymbol{\xi}) = \sum_{k \in K} A_k \Phi_k(\boldsymbol{\xi})\,, \tag{3}$$

in which $\{A_k\}_{k \in K}$ are the set of stochastic modes, and $\{\Phi_k(\boldsymbol{\xi})\}_{k \in K}$ are the set of basis functions spanning the uncertainty space $\boldsymbol{\xi}$. As an example, the uncertain Manning's parameter can be initialised with a uniform probability distribution given by:

$$n_\mathrm{M}(\boldsymbol{\xi}) = \overline{n_\mathrm{M}} + \delta_{n_\mathrm{M}} \xi_1\,, \tag{4}$$

with mean value $\overline{n_{\mathrm{M}}}$, and uniform uncertainty range $\delta_{n_{\mathrm{M}}}$ assigned to the uncertainty dimension $\xi_1 \in [-1, 1]$. The k^{th} stochastic mode $n_{\mathrm{M}k}$ is then initialised by a projection of Eq. (4) onto the k^{th} basis function Φ_k:

$$n_{\mathrm{M}k} = \langle n_{\mathrm{M}}(\boldsymbol{\xi})\Phi_k(\boldsymbol{\xi})\rangle \ , \tag{5}$$

where $\langle\cdot\rangle$ is the so-called *expectation operator*, defined as the mean value (or expected value) over the uncertainty space. When Haar wavelet basis functions are chosen, the expectation operator can be approximated by a Haar wavelet quadrature rule, as described later in section 2.3.3.

2.2. Stochastic modes and their evolution operators

Having initialised the uncertain model inputs, each flow vector $\mathbf{U}^n_{i,k} = \left[h^n_{i,k}, q^n_{i,k}\right]^{\mathsf{T}}$ over physical element i has a set of stochastic modes $k \in K$ that are evolved by the following set of decoupled finite volume stochastic operators:

$$\mathbf{U}^{n+1}_{i,k} = \mathbf{U}^n_{i,k} - \Delta t\left(\frac{\left\langle\widetilde{\mathbf{F}}^n_{i+1/2}\Phi_k(\boldsymbol{\xi})\right\rangle - \left\langle\widetilde{\mathbf{F}}^n_{i-1/2}\Phi_k(\boldsymbol{\xi})\right\rangle}{\Delta x} - \mathbf{S}_{\mathrm{b}}{}^n_{i,k}\right), \tag{6}$$

where $\widetilde{\mathbf{F}}^n_{i+1/2}$ is the deterministic numerical flux at interface $i + 1/2$ between physical elements i and $i + 1$, calculated using a Roe approximate Riemann solver (Roe and Pike, 1985). Frictional effects are applied separately to each stochastic mode using the splitting implicit scheme of Liang and Marche (2009) (see Appendix B). In Eq. (6), the k^{th} stochastic mode of the bed slope source term, $\mathbf{S}_{\mathrm{b}}{}^n_{i,k}$, involves the product of water depth and topography slope, and so it is calculated by the so-called *pseudo-spectral product operator* (see Appendix A):

$$\mathbf{S}_{\mathrm{b}}{}^n_{i,k} = \left[0, -g\sum_{r\in K}\sum_{s\in K}\left(\frac{h^{+,\star}_{i-1/2,r} + h^{-,\star}_{i+1/2,r}}{2}\right)\left(\frac{z^{-,\dagger}_{i+1/2,s} - z^{+,\dagger}_{i-1/2,s}}{\Delta x}\right)\langle\Phi_r\Phi_s\Phi_k\rangle\right]^{\mathsf{T}} \tag{7}$$

where variables marked with $\star$ and $\dagger$ are given in Appendix B, and involve local and nonlinear max() operations to preserve depth positivity and well-balancedness in the deterministic case (Liang and Marche, 2009). The expectations of numerical fluxes $\left\langle\widetilde{\mathbf{F}}^n_{i\pm1/2}\Phi_k(\boldsymbol{\xi})\right\rangle$ in Eq. (6) are evaluated by the Haar wavelet quadrature rule described later in section 2.3.3. The expectation $\langle\Phi_r\Phi_s\Phi_k\rangle$ in Eq. (7) can be precalculated and stored during model initialisation (see Appendix A).

2.3. Choice of basis to span the uncertainty space

In principle, any basis can be chosen to span the uncertainty space but, in practice, robustness and stability cannot be guaranteed with a global polynomial basis, as demonstrated by Shaw and Kesserwani (2020). Here, multidimensional Haar wavelet basis functions are selected to provide a localised, piecewise-constant decomposition spanning the space of multiple uncertainty dimensions. Haar wavelet basis functions have already been adopted for hyperbolic conservation laws without source terms, being favoured for their reliable capture of probability distributions functions with discontinuities (Le Maître et al., 2004a; Pettersson et al., 2014). Such distributions arise at points where the flow is highly nonlinear (Shaw and Kesserwani, 2020; Abgrall and Mishra, 2017), and are particularly expected at uncertain wet-dry fronts where there is a high probability of zero depth and low probabilities of positive depths. The construction of the Haar wavelet basis functions is presented first for a single uncertainty dimension in section 2.3.1, then extended into arbitrarily high dimensionality in section 2.3.2.

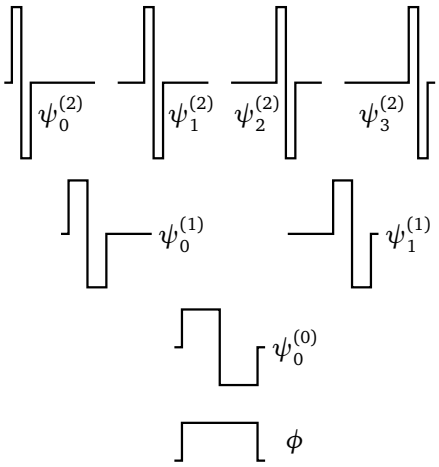

Fig. 1. 1D Haar wavelet basis with maximum refinement level $L = 3$, having eight basis functions spanning the space of uncertainty, $\xi \in [-1, 1]$. The eight basis functions are presented in a tree formation: the father function ϕ (Eq. (8)) is at the root of the tree, and the wavelet functions $\psi_j^{(m)}$ (Eq. (9)) are arranged according to their refinement level (m) and position j.

2.3.1. Representation of one-dimensional uncertainty space

Haar wavelets are multiscale, recursively nested and overlapping basis functions that are constructed by recursive, two-way subdivision of the uncertainty space, up to a maximum refinement level L chosen by the user. For a single source of uncertainty ($D = 1$) and assuming a maximum refinement level $L = 3$ (for simplicity of presentation), the 1D uncertainty space is spanned by $2^3 = 8$ basis functions that are organised recursively into a tree structure, as shown in Fig. 1. A probability distribution defined on the uncertainty space can be represented by assembling all eight basis functions to form a piecewise-constant approximation with eight locally-constant *stochastic elements*. At the root of tree is the so-called father function $\phi(\xi)$:

$$\phi(\xi) = \begin{cases} 1 & \text{if } -1 \le \xi < 1, \\ 0 & \text{otherwise.} \end{cases} \tag{8}$$

At each refinement level $m = 0, \ldots, L-1$, a collection of Haar wavelet basis functions $\psi_j^{(m)}(\xi)$ are defined, where j is the position of the wavelet in the uncertainty space at refinement level (m) [1]. The Haar wavelet basis functions $\psi_j^{(m)}(\xi)$ are defined as:

$$\begin{aligned} \psi_j^{(m)}(\xi) &= 2^{m/2}\,\psi(2^m(\xi+1) - 2j - 1)\ , \\ m &\in 0, \ldots, L-1\ ;\ j \in 0, \ldots, 2^m - 1\ , \end{aligned} \tag{9}$$

[1] For clarity of notation, a refinement level is denoted as superscript (m) with parentheses in order to distinguish it from a time level denoted as superscript n without parentheses.

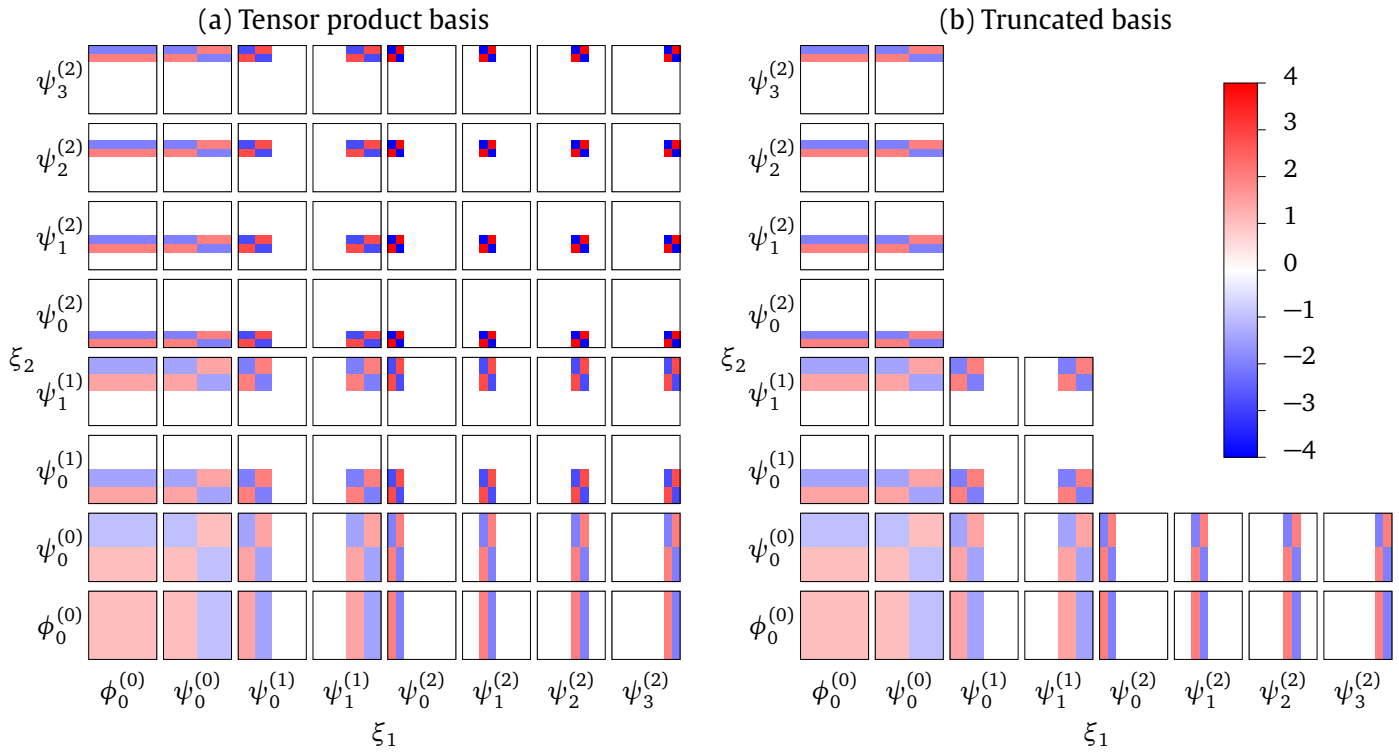

Fig. 2. 2D Haar wavelet (a) tensor product basis and (b) truncated basis. Both bases have a maximum refinement level $L = 3$. Each square panel shows a basis function defined over the 2D uncertainty space $\boldsymbol{\xi} \in [-1, 1] \times [-1, 1]$. The generalisation to arbitrarily high dimensionality is given in Appendix A.

which are a translation and dilation of the so-called mother function $\psi(\xi)$:

$$\psi(\xi) = \begin{cases} 1 & \text{if } -1 \leq \xi < 0, \\ -1 & \text{if } 0 \leq \xi < 1, \\ 0 & \text{otherwise.} \end{cases} \tag{10}$$

Equipped with the set of Haar wavelet basis functions, any stochastic variable $A(\xi)$ can be written as a Haar wavelet basis expansion by starting with the mean value $\overline{A}$, then recursively summing successively fine-scale features in the probability distribution represented by the stochastic modes $A_j^{(m)}$:

$$A(\xi) = \overline{A}\,\phi(\xi) + \sum_{m=0}^{L-1} \sum_{j=0}^{2^m-1} A_j^{(m)} \psi_j^{(m)}(\xi)\,. \tag{11}$$

which can be simplified to obtain Eq. (3) by adopting the notation given in Appendix A.

2.3.2. Representation of D-dimensional uncertainty space

For multiple sources of uncertainty ($D > 1$), the D uncertainty dimensions can be spanned either by a D-dimensional tensor product of 1D basis functions with 2^{DL} stochastic modes, or by a D-dimensional truncated basis with a substantially reduced number of stochastic modes. Basis truncation is commonly recommended to reduce the computational cost for hyperbolic conservation laws without source terms (Le Maître et al., 2004a; Xiu and Karniadakis, 2002; Blatman and Sudret,

2011), and has been proven to preserve robustness in the deterministic case for a discontinuous Galerkin hydrodynamic model (Kesserwani et al., 2018). However, basis truncation has yet to be applied in an intrusive hydrodynamic model and, accordingly, this study examines the validity of truncation for preserving robustness measures associated with bed slope and friction source terms.

With two uncertainty dimensions ($D = 2$) and maximum refinement level $L = 3$, the 2D tensor product basis shown in Fig. 2a has 64 Haar wavelet basis functions and 64 corresponding stochastic modes. The 1D father function ϕ and 1D wavelet functions $\psi_j^{(m)}$ span the two uncertainty dimensions ξ_1 and ξ_2, and the 8×8 panels show the 2D Haar wavelet basis functions formed by a tensor product of the 1D functions. Each panel spans the entire uncertainty space, $\boldsymbol{\xi} \in [-1, 1] \times [-1, 1]$. The same arrangement of 2D Haar wavelet basis functions is shown for the truncated basis in Fig. 2b. Basis truncation is achieved by removing the 32 basis functions representing fine-scale cross-dependencies, leaving only 32 remaining. Hence, for this choice of D and L, basis truncation achieves a 50% reduction in the number of basis functions and stochastic modes. The generalisation of basis truncation to arbitrarily high D-dimensional uncertainty space is defined in Appendix A.

The tensor product basis enables robustness measures to be effortlessly transferred from the deterministic context into the D-dimensional uncertainty space: due to the locality of Haar wavelets, the uncertainty dimensions become decoupled from the physical dimensions, ensuring that stochastic discretisation errors, which are governed solely by the choice of L, do not interfere with physical discretisation errors, which are governed solely by the underlying deterministic formulation. This decoupling means that nonlinear operations within the stochastic finite volume operators are calculated exactly over each locally-constant stochastic element.

With the truncated basis, stochastic modes representing the cross-dependencies at fine scales are intentionally removed. This leads to stochastic truncation errors in the uncertainty dimensions which can propagate into the physical dimension due to nonlinear operations within the robustness measures and probabilistic Riemann flux evaluations (see section 2.3.3). The potential impact of stochastic truncation error propagation will be studied later in section 4.1.

2.3.3. Approximate solution of the probabilistic Riemann problem

A compatible Haar wavelet quadrature rule is now required to evaluate the nonlinear terms within the stochastic finite volume operators (Eq. (6)), including the approximate solution of the probabilistic Riemann problem. The 2^{DL} quadrature points $\boldsymbol{\xi}_{\mathbf{p}}$ are positioned at the centres of the locally-constant stochastic elements:

$$\boldsymbol{\xi}_{\mathbf{p}} = \frac{\Delta\boldsymbol{\xi}}{2} + \mathbf{p} \cdot \Delta\boldsymbol{\xi} - \{1\}^D \,, \;\; \mathbf{p} \in \mathbf{P}, \tag{12}$$

where $\Delta\boldsymbol{\xi} = \{2/2^L\}^D$, and $\mathbf{P} = \{0, \ldots, 2^L - 1\}^D$ which is the index set of stochastic elements. The quadrature weight $w = 2^D/2^{DL}$ is the size of a stochastic element, and the quadrature rule is defined as:

$$\begin{aligned} A_k &= \langle A(\boldsymbol{\xi})\Phi_k(\boldsymbol{\xi})\rangle \\ &= \frac{1}{2^D} \int_{[-1,1]^D} A(\boldsymbol{\xi})\, \Phi_k(\boldsymbol{\xi})\, \mathrm{d}\boldsymbol{\xi} \approx \frac{1}{2^D} \sum_{\mathbf{p}\in\mathbf{P}} w\, A(\boldsymbol{\xi}_{\mathbf{p}})\, \Phi_k(\boldsymbol{\xi}_{\mathbf{p}})\,, \end{aligned} \tag{13}$$

which can be used to calculate the k^{th} stochastic mode of any quantity $A(\boldsymbol{\xi})$ (see Appendix A). In particular, the Haar wavelet quadrature rule given by Eq. (13) is used to evaluate the expectation of the numerical flux $\left\langle \widetilde{\mathbf{F}}^n_{i+1/2} \Phi_k(\boldsymbol{\xi}) \right\rangle$ that appears

in Eq. (6):

$$\left\langle \widetilde{\mathbf{F}}^{n}_{i+1/2}\Phi_k(\boldsymbol{\xi})\right\rangle \approx \frac{1}{2^D}\sum_{\mathbf{p}\in\mathbf{P}} w\,\widetilde{\mathbf{F}}\left(\mathbf{U}^{-,\star}_{i+1/2}(\boldsymbol{\xi}_{\mathbf{p}}),\mathbf{U}^{+,\star}_{i+1/2}(\boldsymbol{\xi}_{\mathbf{p}})\right)\Phi_k(\boldsymbol{\xi}_{\mathbf{p}}), \tag{14}$$

where flow vectors marked with $\star$ are modifications of the original flow vectors, which are designed to preserve well-balancedness. Nonlinear terms that appear in the wetting-and-drying treatment and friction scheme are also evaluated by the same quadrature rule (see Appendix B). The quadrature points given by Eq. (12) are reused to initialise an alternative nonintrusive counterpart, which is formulated next in section 3.

3. Formulation of the nonintrusive counterpart

A nonintrusive model is formulated that shares the same Haar wavelet basis and initialisation procedure as the intrusive model. The nonintrusive model deterministically samples at the same Haar wavelet quadrature points given by Eq. (12). The nonintrusive model straightforwardly preserves the same physical discretisation error as the underlying deterministic model, and the stochastic discretisation error is determined solely by the maximum refinement level L. Hence, the nonintrusive model has the same model structural error as the intrusive model using a Haar wavelet tensor product basis (section 2.3.2), with both models yielding identical outputs.

4. Numerical results

Four numerical tests are conducted to assess the robustness, efficiency, and reliability of the intrusive and nonintrusive models under multiple sources of uncertainty. The first two tests in section 4.1 verify the robustness of the intrusive model, and determine the validity of basis truncation. The final two tests in section 4.2 measure the computational cost of the intrusive and nonintrusive models against a conventional Monte Carlo approach, and examine the reliability of the wavelet-based formulations to capture fine-scale variations in probability distributions.

4.1. Intrusive model verification under joint uncertainties

Due to the localisation of Haar wavelets, the intrusive formulation with a tensor product basis is expected to inherit the robustness measures of the underlying deterministic model, while basis truncation intentionally ignores fine-scale cross-dependencies between the multiple sources of uncertainty (see section 2.3.2). This section numerically verifies the intrusive model's ability to preserve robust well-balancedness between flux and topography gradients with wetting-and-drying processes and friction effects. Two test cases, each with two sources of uncertainty, are simulated by the intrusive model configured with refinement level $L = 3$, and a tensor product basis or a truncated basis.

4.1.1. Lake-at-rest with uncertain wet and dry zones

This lake-at-rest test (Sharifian et al., 2018) was initially used to verify the well-balancedness of deterministic models for various topographic shapes and steepness levels in the presence of wet/dry zones and fronts. Under a lake-at-rest, an initially still water level should be preserved indefinitely without generating spurious non-zero discharge flow, which is achieved by the underlying deterministic finite volume discretisation (Kesserwani et al., 2019).

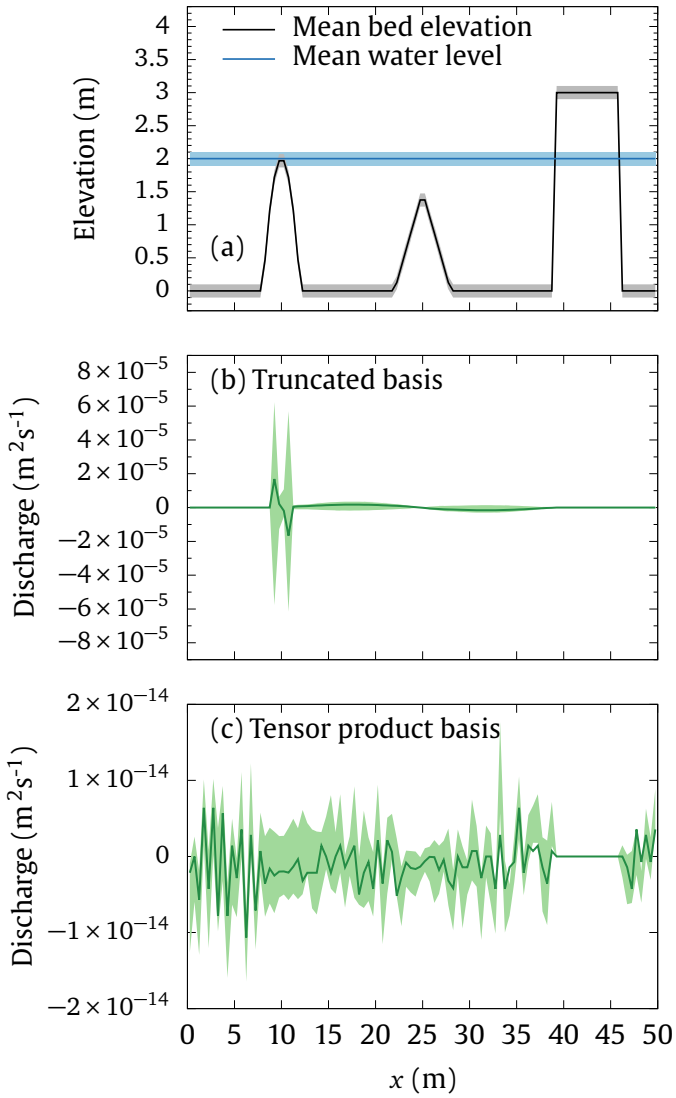

Fig. 3. Lake-at-rest with uncertain wet and dry zones: (a) joint uncertainties in bed elevation and initial water level, with shading indicating the range of uncertainty. The discharge profiles at $t = 100$ s are obtained for the intrusive model using: (b) the truncated basis, and (c) the tensor product basis. Note that discharge scales differ between (b) and (c).

To verify that well-balancedness is preserved by the intrusive model, a probabilistic variant of this test is proposed by perturbing the initial water elevation and topography so that both are uncertain. The mean topography is given in Sharifian et al. (2018), and the mean initial water level is 2 m. Both topography and initial water level are assigned uniform probability distributions with an uncertainty range of ±0.1 m representing 10% measurement errors. This initial configuration is shown in Fig. 3a, which has three topographic obstacles: one rectangular (right), one triangular (middle), and one smooth (left). The rectangular obstacle has 100% certainty of being dry, since any region with negative initial water depth is assumed dry. The triangular obstacle has 100% certainty of being wet, but the water depths themselves are uncertain. The peak of the smooth obstacle is possibly wet or dry, since the initial water level and topographic uncertainties interact. Intrusive models are run with either a truncated or a tensor product basis. Runs are performed on a mesh with 100 cells and are set to end at $t = 100\,\mathrm{s}$, corresponding to 1000 time-steps with $\Delta t = 0.1\,\mathrm{s}$.

The final discharge profiles using the truncated basis (Fig. 3b) and tensor product basis (Fig. 3c) reveal different model behaviour in the vicinity of the rectangular, triangular and smooth obstacles. Around the rectangular obstacle, both intrusive models preserve robustness in this dry region since the flow discharge is zero with 100% certainty, and there is no interdependence between the topographic and water depth uncertainties. In contrast, the uncertain water depth over the triangular and around the smooth obstacles interacts with the topographic uncertainty, making these regions susceptible to basis truncation errors. Near the triangular obstacle, these truncation errors disturb well-balancedness over the wet region, resulting in spurious discharge magnitudes up to $5 \times 10^{-6}\,\mathrm{m^2\,s^{-1}}$. These errors become even larger near the peak of the smooth obstacle, where the region is possibly wet or dry, as the impact basis truncation errors also affect the reliability of the wetting-and-drying treatment. The spurious discharges showed no sign of growth, remaining constant over the 100 s simulation, providing further evidence that they are truncation errors.

Unlike the intrusive model with the truncated basis, the model with the tensor product basis exactly captures a zero probabilistic discharge to machine precision across the entire domain (Fig. 3c), and the initial probabilistic water level stays unperturbed. Hence, the intrusive model with the tensor product basis preserves the same degree of well-balancedness and wetting-and-drying that feature in the underlying deterministic model.

4.1.2. Transient and frictional dam-break flow

Having assessed model robustness under zero-flow, steady-state conditions in section 4.1.1, the same assessment is now made for transient and frictional flow by simulating the flume experiment of a dam-break wave propagating over an initially dry bed and interacting with a triangular obstacle (Hiver, 2000). The test is brought into a probabilistic setting by specifying joint uncertainties in the Manning's roughness parameter and the height of the triangular obstacle.

The domain is 38 m long and the upstream water depth is 0.75 m, dammed by a gate that is instantaneously removed at $t = 0\,\mathrm{s}$, as shown in Fig. 4. The domain is discretised by 114 physical elements such that cell centres are collocated with the depth sensors marked in Fig. 4. Numerically reflective boundary conditions are imposed upstream and transmissive

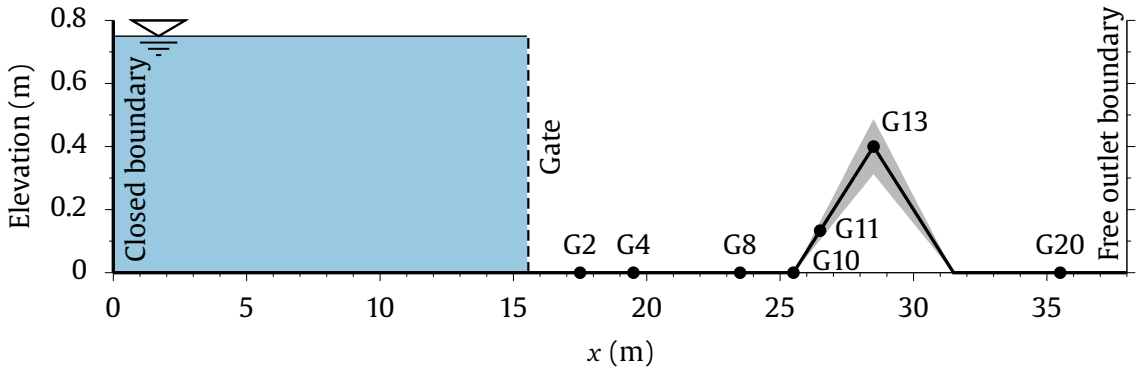

Fig. 4. Transient and frictional dam-break flow. Test setup following Hiver (2000) with seven gauge points marked where experimental water depths are available. The topographic uncertainty introduced is shaded in grey.

boundary conditions downstream. The uncertain topography with a triangular obstacle $z(x, \boldsymbol{\xi})$ is:

$$z(x, \boldsymbol{\xi}) = \frac{\overline{a} + \delta_a \xi_2}{3} \begin{cases} x - 25.5 & \text{if } 25.5 < x \leq 28.5, \\ 31.5 - x & \text{if } 28.5 < x < 31.5, \\ 0 & \text{otherwise,} \end{cases} \tag{15}$$

in which the mean obstacle peak is $\overline{a} = 0.4\,\text{m}$ and the maximum uncertainty range is $\delta_a = 0.1\,\text{m}$. The Manning's roughness parameter has a mean value of $0.012\,\text{s}\,\text{m}^{-1/3}$, which is perturbed by a small uncertainty range of $0.004\,\text{s}\,\text{m}^{-1/3}$ because the material properties in the laboratory are well-known. Intrusive model runs are set to end at $t = 90\,\text{s}$ with a fixed time-step of $\Delta t = 0.04\,\text{s}$, and runs are performed using a tensor product basis or a truncated basis.

Using a truncated basis, the intrusive model crashes as soon as the wetting front reaches the topographic slope at $x = 25.66\,\text{m}$ and $t = 2.96\,\text{s}$. This is the first place and time that the wetting front encounters topography uncertainty, that the flow responds jointly to topographic and frictional uncertainties, and that the intrusive model becomes susceptible to truncation errors. Fig. 5a shows the variation of the water depth variable at $x = 25.66\,\text{m}$ and $t = 2.96\,\text{s}$ in the 2D uncertainty space. Unphysical negative water depths shaded red are caused by stochastic truncation errors, which are responsible for the model crashing. Since the truncated basis ignores fine-scale cross-dependencies between uncertainties, truncation errors manifest as a checkerboard pattern having the same shape as the underlying Haar wavelet basis functions seen in Fig. 2b. Switching to a tensor product basis ensures that the intrusive model correctly preserves probabilistic depth positivity: as seen in Fig. 5b, most of the panel is white, indicating a high probability of a dry cell, unless the Manning's parameter is less than $0.01\,\text{s}\,\text{m}^{-1/3}$ where there is a probability of a wet cell.

The intrusive model with a tensor product basis preserves robustness throughout the 90 s simulation, with time series of its probabilistic water depth predictions shown in Fig. 6 at gauge points G8 (slightly upstream of the obstacle) and G20 (slightly downstream of the obstacle). The experimental data lie within the range of the probabilistic water level prediction, with some small discrepancies observed that are commonly reported for many deterministic hydrodynamic models (Liang and Marche, 2009; Caviedes-Voullième and Kesserwani, 2015; Mao et al., 2016). The slight overprediction at G20 in Fig. 6b could be because the wave pattern in this region becomes complex and unstable and cannot be appropriately captured under

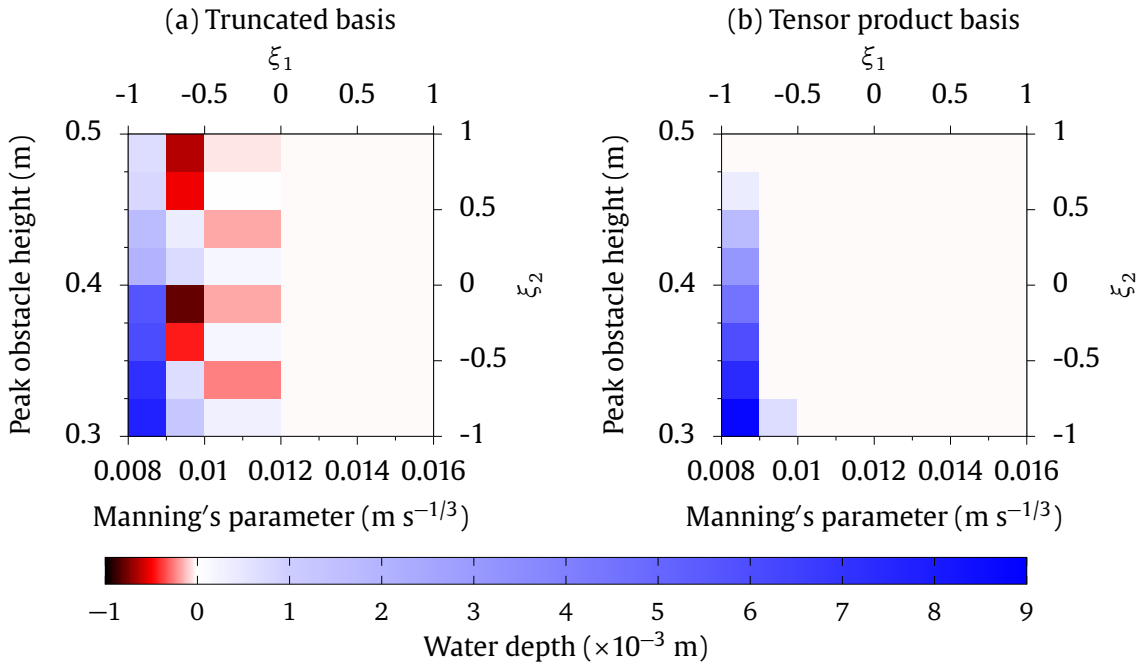

Fig. 5. Transient dam-break and frictional flow. Water depth distribution in the 2D uncertainty space at $x = 25.66$ m and $t = 2.96$ s, the place and time at which the intrusive model with the truncated basis crashes: (a) truncated basis prediction showing negative water depths shaded in red; and, (b) tensor product basis prediction showing that depth positivity is preserved.

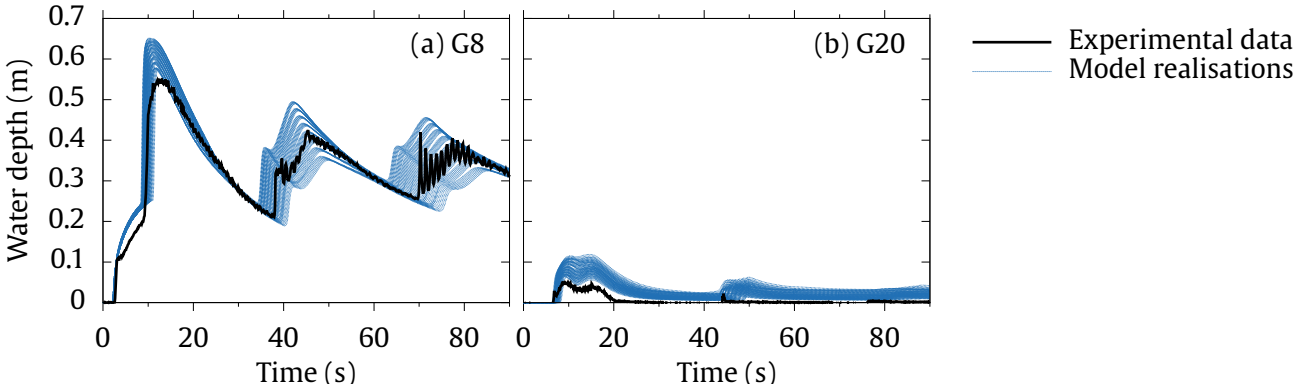

Fig. 6. Transient dam-break and frictional flow. Time series of water depths at gauge points (a) G8, and (b) G20 as marked in Fig. 4. The 64 possible realisations are plotted individually for the intrusive model, configured with a tensor product basis and compared to the (deterministic) experimental data.

the hydrostatic assumption of the shallow water equations.

As shown in Fig. 6, as soon as the dam-break wave first reflects off the triangular obstacle, topographic uncertainty has a major effect on the wave height which, in turn, affects wave speed and arrival time. The reflected wave reaches gauge point G8 around $t = 10$ s, with uncertainty in the arrival time and wave height evident in Fig. 6a. These uncertainties accumulate and extend further across the domain as the wave continues to propagate and reflect off the closed upstream boundary and the obstacle. Wave propagation speed is also affected by the small uncertainty range on the Manning's roughness parameter, which has a relatively small effect on arrival time compared to the rapid model response to topographic uncertainty.

Across both tests, basis truncation was shown to be unreliable because it does not preserve the degree of well-balancedness and depth positivity of the underlying deterministic formulation. Therefore, when adopting an intrusive approach, a tensor product basis is recommended for robust hydraulic modelling applications. In the following section 4.2, the tensor product configuration is selected to examine the intrusive model's ability to reproduce fine-scale, nonlinear variations in probability distributions at critical points associated with probabilistic transcritical flow, and to compare computational efficiency against a nonintrusive counterpart and a conventional Monte Carlo approach.

4.2. Efficient and reliable capture of probability distributions

Predicting the relative frequency of water depth occurrence is important at critical points where the probabilistic flow responds nonlinearly to uncertainties in topography, roughness and inflow discharge. Such predictions are useful in flood frequency analysis (Brodie, 2013) such as upstream of levees to study the probability of flood recurrence. Capturing these probability distributions efficiently and reliably remains an under-investigated aspect of computational hydraulics. In this section, depth probability distributions are examined for two steady flow tests: the first involving frictionless flow over uncertain topography, and the second involving frictional flow and three joint uncertainties. Simulations are set to end when the mean water depth profile has physically converged to a steady-state down to a threshold of 10^{-4} m. In both tests, intrusive and nonintrusive model results are validated against a Monte Carlo ensemble of 2000 model runs, which is the minimum needed to statistically converge on mean and standard deviation water depth statistics to a threshold of 10^{-4} m.

4.2.1. Steady flow over uncertain topography

Shaw and Kesserwani (2020) proposed a test of steady, frictionless flow over uncertain topography. The test was initially designed to identify advantages and shortcomings of an intrusive model formulated with a global Hermite polynomial basis, which restricted the formulation to a linear topography discretisation that can only represent fully-wet domains. Shaw and Kesserwani (2020) confirmed that their intrusive model accurately predicted mean and standard deviation statistics along the longitudinal channel (Fig. 3 in Shaw and Kesserwani (2020)) but, going deeper to the level of pointwise probability distributions, the global polynomial basis was unreliable, predicting probabilities of negative water depths.

This test is re-explored here using the wavelet-based intrusive and nonintrusive models, which preserve the accuracy of local, nonlinear operations and ensure well-balancedness and wetting-and-drying in the probabilistic setting. As specified by Shaw and Kesserwani (2020), a 20 m-wide obstacle is positioned in the middle of a 100 m-long, flat channel. The obstacle has an uncertain height with a mean of 0.6 m and a standard deviation of 0.3 m. The steady inflow discharge is $1.65\,\mathrm{m^2\,s^{-1}}$, and a subcritical water depth of 1.5 m is fixed at the outlet. The test is set to end at $t = 500$ s when steady-state convergence

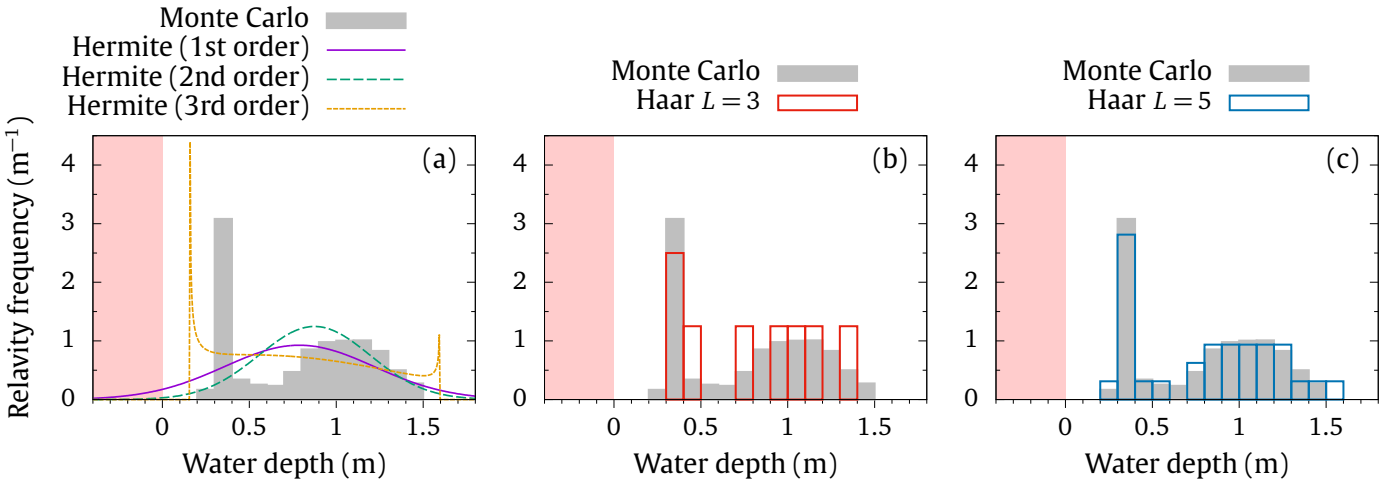

Fig. 7. Steady flow over uncertain topography: water depth probability distributions. The same Monte Carlo histogram is shown in all three panels (a)-(c) and the zone of negative water depths is shaded in red. Panel (a) show existing results of the intrusive model of Shaw and Kesserwani (2020) using 1st, 2nd and 3rd order global Hermite polynomial bases; panels (b) and (c) show results from the wavelet-based intrusive model at refinement level $L = 3$ and $L = 5$, respectively. Results in panels (b) and (c) are also representative of the nonintrusive counterpart, which predicts results identical to the intrusive model.

is reached. Water depth probability distributions are analysed at a point 1.5 m downstream of the obstacle peak, where there is a 50-50 chance of hydraulic jump formation, depending on the obstacle height.

The Monte Carlo histogram is taken as the reference probability distribution, shown in all three panels of Fig. 7. It reveals a bimodal response with one peak around 0.3 m and another around 1 m; this bimodality is due to a strongly nonlinear flow response slightly upstream of the obstacle. As seen in Fig. 7a, the well-balanced intrusive model of Shaw and Kesserwani (2020) was unable to capture the bimodal distribution using low-order global Hermite polynomials. Furthermore, predicted distributions were unreliable because they extended beyond the true range of uncertainty and into the zone of unphysical negative water depths, shaded red in Fig. 7a.

These deficiencies are overcome by the proposed intrusive model and its nonintrusive counterpart: both models calculate identical histograms, and ensure reliable predictions that do not extend beyond the bounds of the Monte Carlo histogram. As seen in Fig. 7b, the overall distribution shape can be captured by the intrusive and nonintrusive models at refinement level $L = 3$ with just eight stochastic modes. Increasing the refinement level to $L = 5$ yields 32 stochastic modes, which is sufficient to accurately reproduce the bimodal distribution (Fig. 7c).

Computational efficiency is analysed by measuring the elapsed CPU times of the intrusive and nonintrusive models at refinement levels between $L = 1$ and $L = 5$, then comparing these measurements against a single deterministic model run, as shown in Fig. 8. The cost of the nonintrusive model is directly proportional to the number of modes: a nonintrusive model run at refinement level L is 2^L times slower than the underlying deterministic model. In this test with a single uncertainty dimension, the intrusive model is about 10%–20% faster than the nonintrusive model, which can be attributed to additional preprocessing and postprocessing overheads in the nonintrusive model. Relative model efficiencies are revisited in the next test in Section 4.2.2 that involves frictional flow with three uncertain dimensions.

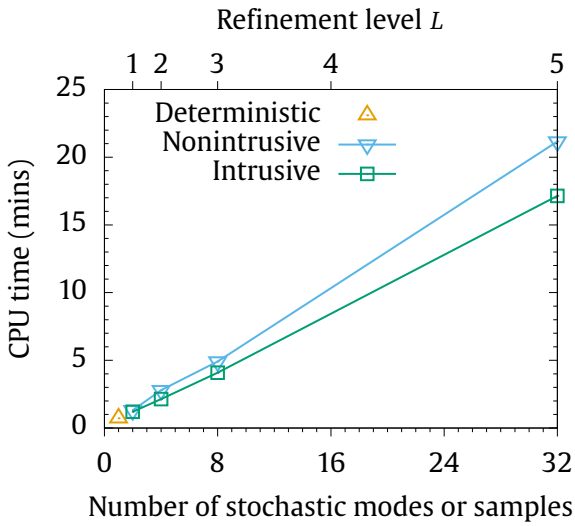

Fig. 8. Steady flow over uncertain topography: CPU times are measured for the intrusive and nonintrusive models at refinement levels $L = 1, 2, 3$ and 5. The CPU time for a single deterministic model run is also marked for comparison.

4.2.2. Steady flow with three joint uncertainties

Tseng (2004) initially proposed a deterministic test of steady transcritical flow over irregular bed topography, flowing downhill along a 1600 m reach of an imaginary river. This test is extended into a probabilistic setting to study the flow response to three joint uncertainties. Three uncertainty dimensions are associated with an error range for the inflow discharge, a range of choices for the Manning's roughness parameter, and a downstream portion of the river bed where there is uncertainty on river bed height potentially caused by sediment transport processes. The steady inflow discharge has 15% uncertainty (Bates et al., 2014), leading to an inflow of $0.59 \pm 0.09\,\mathrm{m^2\,s^{-1}}$. The Manning's parameter is uniform along the entire reach and is taken to be in the range $0.033 \pm 0.01\,\mathrm{s\,m^{-1/3}}$, which is a suitable range for river modelling. A bed uncertainty perturbation $\delta_z(x)$ is introduced along a portion 184 m in length, where deposition or erosion effects could be significant (see Fig. 9a), and is defined as:

$$\delta_z(x) = \delta_{z0} \begin{cases} \frac{x-1184}{80} & \text{if } 1184 < x \leq 1264, \\ \frac{1368-x}{104} & \text{if } 1264 < x \leq 1368, \\ 0 & \text{otherwise}, \end{cases} \tag{16}$$

with a maximum uncertainty scaling of $\delta_{z0} = 0.5$ m. The water depth at the outlet boundary is fixed at 0.42 m. The physical domain is discretised by 200 cells ($\Delta x = 8$ m) and the time-step is fixed at $\Delta t = 0.4$ s. All simulations start from an initially dry bed with the inflow filling the domain gradually, ending when steady-state convergence is reached at $t = 5000$ s.

The intrusive model is configured with refinement level $L = 2$ resulting in $4 \times 4 \times 4 = 64$ stochastic modes and a probabilistic solution with 64 realisations as shown in Fig. 9b. Water depth uncertainties of about 0.2 m are found throughout the entire reach due to inflow and friction uncertainties, whereas relatively large water depth uncertainties up to 1 m are found just upstream of the uncertain bed portion.

The nonintrusive model obtained identical results with 64 modes identical to Fig. 9b, but completed the same simulation

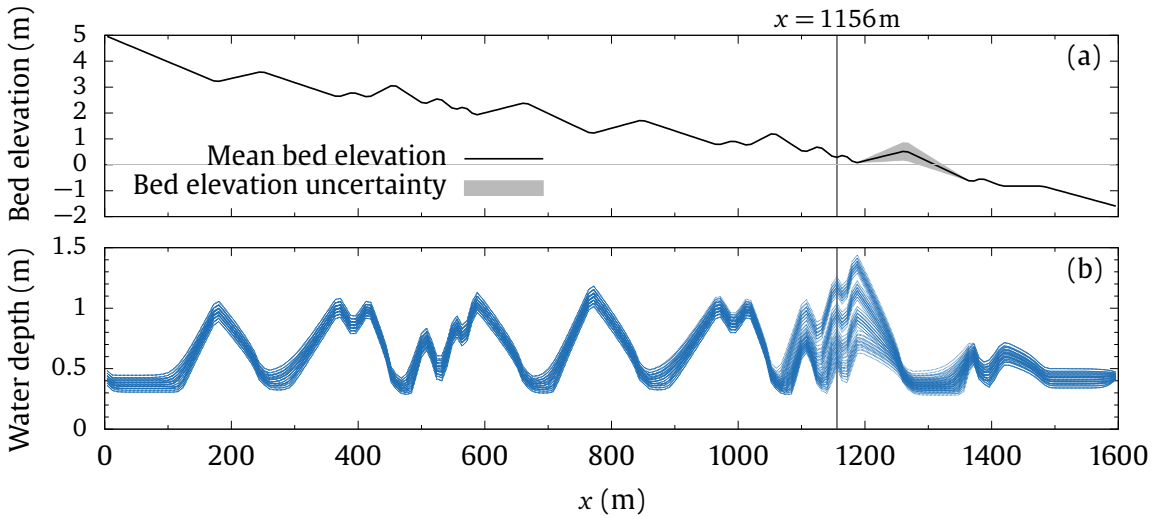

Fig. 9. Probabilistic steady-state solution with three joint uncertainties: (a) uncertain bed profile with the mean bed elevation specified by Tseng (2004) and a 184 m portion of uncertainty shaded grey; (b) probabilistic water depth profile predicted by the intrusive model at refinement level $L = 2$, comprising 64 realisations plotted individually. A vertical line at $x = 1156$ m marks the position of the water depth histograms shown in Fig. 10.

2.4 times faster than the intrusive model. The intrusive model is slower due to overheads in quadrature evaluation, which become substantial in three uncertainty dimensions, and dwarf the minor efficiency gains seen in Fig. 8 for the previous steady flow test with a single uncertainty dimension. Given this relative inefficiency, and given both intrusive and nonintrusive models yield identical predictions outcomes, only the nonintrusive model is considered in the subsequent analysis.

Water depth histograms are analysed at $x = 1156$ m (marked by a vertical line in Fig. 9) located in the portion where the water depth uncertainty is largest. The Monte Carlo histogram is taken as the reference probability distribution, shown in both panels of Fig. 10. Fine-scale variations in the Monte Carlo histogram arise from the nonlinear flow response to an uneven bed and the three joint uncertainties. As seen in Fig.10a, the histogram predicted by the nonintrusive model at refinement level $L = 2$ does not accurately match the Monte Carlo histogram because it only has 64 modes on the $4 \times 4 \times 4$ stochastic grid, which is too coarse to capture the fine-scale variations arising from the three joint uncertainties. Increasing the refinement level to $L = 3$ yields 512 modes on a finer $8 \times 8 \times 8$ stochastic grid, leading to an accurate reproduction of the Monte Carlo histogram (Fig. 10b).

Efficiency analysis from the previous test in section 4.2.1 established that the cost of the nonintrusive model equals the cost of the underlying deterministic model multiplied by the number of samples. The nonintrusive model gains efficiency over Monte Carlo by reducing the required sample size. In this test, the nonintrusive model at refinement level $L = 2$ with 64 modes is 31 times faster than the Monte Carlo ensemble with 2000 samples. At refinement level $L = 3$ with 512 modes, the nonintrusive model is 3.9 times faster.

Across both steady flow tests, the wavelet-based intrusive and nonintrusive models predict reliable probability distributions that remain within the bounds of reference Monte Carlo distributions and preserve depth positivity. However, capturing probability distributions with bimodal responses requires at least a refinement level $L = 3$ per uncertain input for

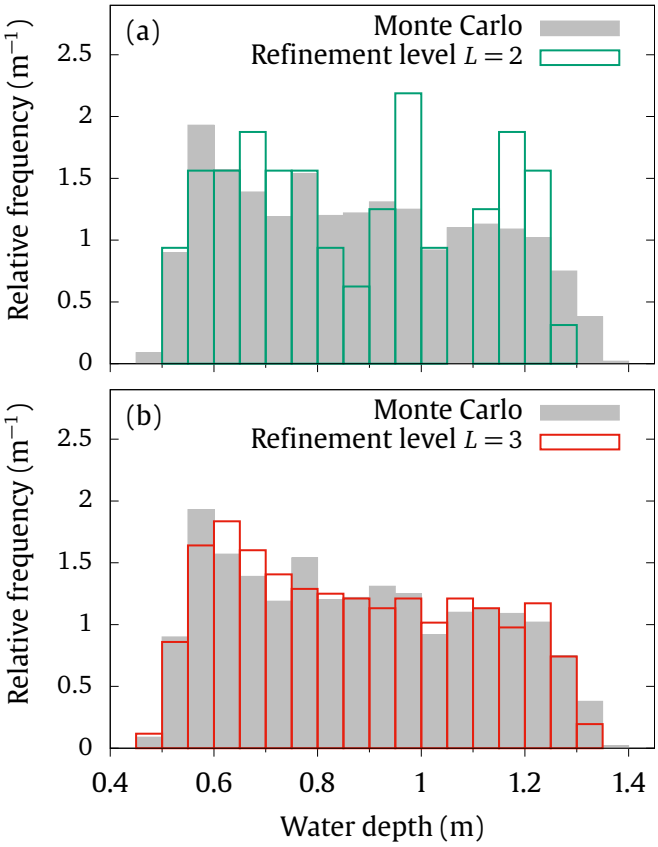

Fig. 10. Histograms of steady-state water depth with three joint uncertainties, calculated at $x = 1156$ m (marked by a vertical line in Fig. 9). The Monte Carlo reference solution is plotted in both panels; overlaid are the nonintrusive solutions at refinement levels (a) $L = 2$, and (b) $L = 3$.

frictional flows, and up to $L = 5$ when flow nonlinearities are strongest, as they are in the frictionless case in Section 4.2.1. When modelling realistic scenarios with multiple sources of uncertainty, the nonintrusive approach is recommended over the intrusive approach because it achieves identically accurate solutions at a substantially lower cost, and offers flexibility for use with any existing deterministic solver.

5. Summary and conclusions

This work adopted an intrusive stochastic Galerkin approach to extend a robust, deterministic Godunov-type hydrodynamic model into a probabilistic setting under D sources of uncertainty. Joint uncertainties in all model variables (water depth, discharge, topography and roughness parameter) were represented by multiscale basis functions formed by a tensor product of Haar wavelets to localise and decouple the space of D uncertainty dimensions from the physical spatial dimension. This decoupling enabled local, nonlinear operations — essential to achieve well-balancedness, wetting-and-drying, and stable friction integration schemes — to be effortlessly extended from the deterministic discretisation into the intrusive model while avoiding any additional discretisation errors. Thus, physical discretisation errors are governed solely by the deterministic discretisation, while stochastic discretisation errors are governed solely by a maximum refinement level L chosen by the user. In this configuration, the intrusive formulation stores and evolves 2^{DL} stochastic modes per physical element, using a Haar wavelet quadrature rule to approximate Riemann problem solutions across the physical and stochastic elements.

Two alternatives were proposed to gain further efficiencies beyond the D-dimensional tensor product basis: either by truncating the tensor product basis to substantially reduce the number of stochastic modes below 2^{DL}, or by adopting a nonintrusive stochastic collocation method to sample the deterministic model 2^{DL} times at the Haar wavelet quadrature points. Probabilistic numerical tests with multiple sources of uncertainty were designed to verify the robustness of the intrusive model with a tensor product or a truncated basis, and to examine the accuracy and efficiency of the intrusive and nonintrusive models in reproducing fine-scale, nonlinear variations in pointwise water depth probability distributions as compared against a conventional Monte Carlo approach.

The probabilistic numerical tests provide new evidence that a tensor product basis must be chosen to preserve robustness measures from the underlying deterministic discretisation into the intrusive formulation. With the truncated basis, the intrusive model could not deliver reliable predictions when the probabilistic flow interacted jointly with multiple sources of uncertainty. With a tensor product basis, a comparative analysis between intrusive and nonintrusive models indicated that a refinement level of at least $L = 3$ was needed to capture fine-scale nonlinear variations in pointwise probability distributions at an accuracy comparable to a statistically-converged Monte Carlo ensemble. The intrusive and nonintrusive models yield predictions of identical accuracy, but the nonintrusive model was found to be more efficient in tests involving multiple sources of uncertainty ($D > 1$). For a more practical test with three sources of uncertainty ($D = 3$), the Monte Carlo ensemble required 2000 model runs, while the nonintrusive model required just 512. Given its efficiency, robustness, and flexibility to be used with any deterministic model, the wavelet-based nonintrusive approach is advantageous for propagating multiple uncertainties in practical hydrodynamic modelling applications.

6. Declaration of interests

The authors declare that they have no known competing financial interests or personal relationships that could have appeared to influence the work reported in this paper.

7. CRediT authorship contribution statement

James Shaw: Conceptualization, Methodology, Software, Investigation, Writing - original draft. **Georges Kesserwani**: Conceptualization, Methodology, Writing - review & editing, Supervision, Project administration, Funding acquisition. **Per Pettersson**: Conceptualization, Methodology.

8. Acknowledgements

Funding: This work was supported by the UK Engineering and Physical Sciences Research Council (EPSRC) grant EP/R007349/1. It is part of the SEAMLESS-WAVE project (SoftwarE infrAstructure for Multi-purpose fLood modElling at variouS scaleS based on WAVElets). For information about the SEAMLESS-WAVE project visit `https://www.seamlesswave.com`. We thank Paul Bates (University of Bristol), Brett Sanders (University of California, Irvine), Domenico Bau and Janice Ayog (The University of Sheffield), Onno Bohove (University of Leeds), and Chris Keylock (Loughborough University) for their beneficial feedback.

Appendix A. Definition of the Haar wavelet basis

The multiscale expansion given by Eq. (11) can be written more succinctly by defining basis functions $\{\Phi_k(\xi)\}_{k\in\{0,\dots,2^L-1\}}$, where the zeroth basis function $\Phi_0(\xi)$ is the father function $\phi(\xi)$ given by Eq. (8), and subsequent basis functions with index $k > 0$ are the Haar wavelet functions given by Eq. (9):

$$\Phi_k(\xi) = \begin{cases} \phi(\xi) & \text{if } k = 0, \\ \psi_j^{(m)}(\xi) & \text{if } k > 0. \end{cases} \tag{A.1}$$

When $k > 0$, a one-to-one mapping is defined from a refinement level m and position j to the basis function index k:

$$k(m, j) = 2^m + j\,, \tag{A.2}$$

which can be inverted to calculate m and j from k:

$$m = \lfloor \log_2(k) \rfloor\,, \tag{A.3a}$$

$$j = k - 2^m\,. \tag{A.3b}$$

Equipped with this notation, Eq. (11) can be rewritten as:

$$A(\xi) = \sum_{k=0}^{2^L-1} A_k \Phi_k(\xi)\,, \tag{A.4}$$

where A_k are the stochastic modes and A_0 is the mean value $\overline{A}$. By taking a tensor product of 1D Haar wavelet basis functions, the D-dimensional tensor product basis is constructed as $\{\Phi_{\mathbf{k}}\}_{\mathbf{k}\in\{0,\ldots,2^L-1\}^D}$, and $A(\boldsymbol{\xi})$ can then be written using multi-index notation as:

$$A(\boldsymbol{\xi}) = \sum_{\mathbf{k}\in\{0,\ldots,2^L-1\}^D} A_{\mathbf{k}}\Phi_{\mathbf{k}}(\boldsymbol{\xi})\,. \tag{A.5}$$

Multidimensional basis truncation

A multidimensional truncated basis is constructed by calculating the total refinement level for each tensor product basis function, where the total refinement level $m_{\text{tot}}(\mathbf{k})$ is defined as (Le Maître et al., 2004a)

$$m_{\text{tot}}(\mathbf{k}) = \sum_{d=1}^{D} m(k_d)\,, \tag{A.6}$$

in which $m(k_d)$ is given by Eq. (A.3a). The truncated basis retains only those basis functions with $m_{\text{tot}}(\mathbf{k}) < L$. Hence, the truncated basis expansion of $A(\boldsymbol{\xi})$ is

$$A(\boldsymbol{\xi}) = \sum_{\substack{\mathbf{k}\in\{0,\ldots,2^L-1\}^D \\ m_{\text{tot}}(\mathbf{k})<L}} A_{\mathbf{k}}\Phi_{\mathbf{k}}(\boldsymbol{\xi}_{\mathbf{k}})\,, \tag{A.7}$$

where $\Phi_{\mathbf{k}}, \left\{\mathbf{k}\in\{0,\ldots,2^L-1\}^D : m_{\text{tot}}(\mathbf{k}) < L\right\}$ is the truncated basis. The number of stochastic modes is given by the following expression:

$$\sum_{m=0}^{L-1}\sum_{\mathbf{b}\in B_m}\prod_{d=1}^{D} 2^{\max(b_d,1)}\,, \tag{A.8}$$

in which B_m is the set containing all combinations of refinement levels that sum to m, which is given by

$$B_m = \left\{\mathbf{b} = [b_1,\ldots,b_D]^\intercal \in \mathbb{N}_0^D : \sum_{d=1}^{D} b_d = m\right\}. \tag{A.9}$$

Simplified indexing

To simplify presentation, basis function indexing is 'flattened' by using $k \in K$ as shorthand for the basis function indices belonging to the index set K, and $\Phi_k(\boldsymbol{\xi})$ as shorthand for the basis functions themselves. Using this notation, $A(\boldsymbol{\xi})$ becomes:

$$A(\boldsymbol{\xi}) = \sum_{k\in K} A_k\Phi_k(\boldsymbol{\xi})\,, \tag{A.10}$$

where the basis $\{\Phi_k(\boldsymbol{\xi})\}_{k\in K}$ may be any tensor product or truncated basis. Since the zeroth stochastic mode A_0 is the mean value $\overline{A}$, then the zeroth basis function is the product of the father functions ϕ such that $\Phi_0(\boldsymbol{\xi}) = \phi(\xi_1)\times\cdots\times\phi(\xi_D)$. The indexing of the other basis functions is arbitrary.

Properties of the expectation operator

Due to basis orthogonality, the expectation operator $\langle A(\boldsymbol{\xi})\rangle$ can project a stochastic variable $A(\boldsymbol{\xi})$ onto a basis function $\Phi_k(\boldsymbol{\xi})$ such that the k^{th} stochastic mode is $A_k = \langle A(\boldsymbol{\xi})\,\Phi_k(\boldsymbol{\xi})\rangle$. Due to linearity of integration, the expectation operator is distributive over summation, so the projection of $A(\boldsymbol{\xi}) + B(\boldsymbol{\xi})$ onto $\Phi_k(\boldsymbol{\xi})$ is

$$\left\langle\left[A(\boldsymbol{\xi}) + B(\boldsymbol{\xi})\right]\Phi_k(\boldsymbol{\xi})\right\rangle = \langle A(\boldsymbol{\xi})\Phi_k(\boldsymbol{\xi})\rangle + \langle B(\boldsymbol{\xi})\Phi_k(\boldsymbol{\xi})\rangle\,, \tag{A.11}$$

and, if $A(\boldsymbol{\xi})$ and $B(\boldsymbol{\xi})$ are basis expansions, then

$$\langle [A(\boldsymbol{\xi}) + B(\boldsymbol{\xi})]\, \Phi_k(\boldsymbol{\xi}) \rangle = A_k + B_k. \tag{A.12}$$

Also due to linearity of integration, a constant factor c can be separated from the expectation:

$$\langle cA(\boldsymbol{\xi}) \rangle = c \langle A(\boldsymbol{\xi}) \rangle . \tag{A.13}$$

Pseudo-spectral product operator

Given stochastic variables $A(\boldsymbol{\xi})$ and $B(\boldsymbol{\xi})$, the product $C(\boldsymbol{\xi}) = A(\boldsymbol{\xi})B(\boldsymbol{\xi})$ can be calculated by a pseudo-spectral product (Debusschere et al., 2004), where the k^{th} stochastic mode C_k is calculated as:

$$\begin{aligned} C_k &= \langle A(\boldsymbol{\xi})B(\boldsymbol{\xi})\Phi_k(\boldsymbol{\xi}) \rangle \\ &= \left\langle \left(\sum_{r \in K} A_r \Phi_r \right) \left(\sum_{s \in K} B_s \Phi_s \right) \Phi_k \right\rangle . \end{aligned} \tag{A.14}$$

Due to linearity of integration and distributivity of summation, the stochastic mode C_k becomes

$$C_k = \sum_{r \in K} \sum_{s \in K} A_r B_s \langle \Phi_r \Phi_s \Phi_k \rangle . \tag{A.15}$$

In general, the pseudo-spectral product only approximates the true product because the set of basis functions required to exactly represent $C(\boldsymbol{\xi})$ may be larger than the set required to represent $A(\boldsymbol{\xi})$ or $B(\boldsymbol{\xi})$ alone (Debusschere et al., 2004). However, in the special case of a 1D or tensor product Haar wavelet basis, the pseudo-spectral product is exact (Le Maître et al., 2004a).

The expectation of the triple basis product $\langle \Phi_r \Phi_s \Phi_k \rangle$ is calculated exactly using the quadrature rule in Eq. (13):

$$\langle \Phi_r \Phi_s \Phi_k \rangle = \sum_{\mathbf{p} \in \mathbf{P}} w\, \Phi_r(\boldsymbol{\xi}_\mathbf{p})\, \Phi_s(\boldsymbol{\xi}_\mathbf{p})\, \Phi_k(\boldsymbol{\xi}_\mathbf{p}) . \tag{A.16}$$

Eq. (A.16) evaluates to zero for many combinations of (r, s, k), and the number of non-zero triple basis products is $\left(4 + 3(L-1)2^L\right)^D$ for any tensor product basis. Since Eq. (A.16) is independent of the stochastic variables and involves only basis functions, it can be precalculated and non-zero values can be stored during model initialisation.

Appendix B. Specification of the evolution operators

The intrusive evolution operators were summarised in section 2.2, and their complete description is given here. The frictional force S_f, which is treated separately from other forces, is applied to the k^{th} stochastic mode of the discharge variable as (Liang and Marche, 2009):

$$q_{i,k}^{n+1} = q_{i,k}^n + \left\langle \frac{\Delta t S_{\mathrm{f}i}^{\ n}(\boldsymbol{\xi}_\mathbf{p})}{\mathcal{D}_i^n(\boldsymbol{\xi}_\mathbf{p})} \Phi_k(\boldsymbol{\xi}) \right\rangle, \tag{B.1}$$

where $S_{\mathrm{f}i}^{\ n} = -C_{\mathrm{f}i}^{\ n} u_i^n \left| u_i^n \right|$, the roughness coefficient is $C_{\mathrm{f}i}^{\ n} = g n_\mathrm{M}^2 / \left(h_i^n\right)^{1/3}$, and the implicit operator $\mathcal{D}_i^n$ is

$$\mathcal{D}_i^n = 1 + 2\Delta t C_{\mathrm{f}i}^{\ n} \left| q_i^n \right| / \left(h_i^n\right)^2 . \tag{B.2}$$

Eq. (B.1) is calculated by the quadrature rule in Eq. (13). If the water depth at a quadrature point $\boldsymbol{\xi}_{\mathbf{p}}$ is dry such that $h_i^n(\boldsymbol{\xi}_{\mathbf{p}}) < h_{\text{tol}}$ where $h_{\text{tol}} = 10^{-6}$ m, then the friction term $\Delta t S_{\text{f}_i}^n(\boldsymbol{\xi}_{\mathbf{p}})/\mathcal{D}_i^n(\boldsymbol{\xi}_{\mathbf{p}})$ in equation (B.1) is taken to be zero at that quadrature point.

After applying frictional forces to the discharge variables, the remaining terms are evaluated as given by Eqs. (6) and (7). To ensure well-balancedness and preserve depth positivity with wetting-and-drying, the topography variables and flow variables are temporarily modified at each time step. First, these variables are defined at the negative limit and positive limit of the interface at $x_{i+1/2}$ and, since the first-order finite volume discretisation has piecewise-constant data, then these variables are:

$$z_{i+1/2}^{-}(\boldsymbol{\xi}) = z_i(\boldsymbol{\xi})\ ,\ z_{i+1/2}^{+}(\boldsymbol{\xi}) = z_{i+1}(\boldsymbol{\xi}), \tag{B.3}$$

$$\mathbf{U}_{i+1/2}^{-}(\boldsymbol{\xi}) = \mathbf{U}_i(\boldsymbol{\xi})\ ,\ \mathbf{U}_{i+1/2}^{+}(\boldsymbol{\xi}) = \mathbf{U}_{i+1}(\boldsymbol{\xi}), \tag{B.4}$$

where the time level n is omitted for clarity of presentation. The water surface elevation $\eta_{i+1/2}^{\kappa}$ and velocity $u_{i+1/2}^{\kappa}$ are then reconstructed, where κ denotes the negative or positive limit:

$$\eta_{i+1/2,k}^{\kappa} = h_{i+1/2,k}^{\kappa} + z_{i+1/2,k}^{\kappa}, \tag{B.5}$$

$$u_{i+1/2}^{\kappa}(\boldsymbol{\xi}_{\mathbf{p}}) = \begin{cases} q_{i+1/2}^{\kappa}(\boldsymbol{\xi}_{\mathbf{p}})/h_{i+1/2}^{\kappa}(\boldsymbol{\xi}_{\mathbf{p}}) & \text{if } h_{i+1/2}^{\kappa}(\boldsymbol{\xi}_{\mathbf{p}}) \geq h_{\text{tol}}, \\ 0 & \text{otherwise.} \end{cases} \tag{B.6}$$

in which $\boldsymbol{\xi}_{\mathbf{p}}$ are the quadrature points given in Eq. (12). To solve the local Riemann problem at $x_{i+1/2}$, a modified topography $z_{i+1/2}^{\star}$ is defined that is made continuous at interfaces by application of the nonlinear max() operator:

$$z_{i+1/2}^{\star}(\boldsymbol{\xi}_{\mathbf{p}}) = \max\left(z_{i+1/2}^{-}(\boldsymbol{\xi}_{\mathbf{p}}), z_{i+1/2}^{+}(\boldsymbol{\xi}_{\mathbf{p}})\right). \tag{B.7}$$

Then, a non-negative water depth $h_{i+1/2}^{\kappa,\star}$ and discharge $q_{i+1/2}^{\kappa,\star}$ are defined that are consistent with the modified topography:

$$h_{i+1/2}^{\kappa,\star}(\boldsymbol{\xi}_{\mathbf{p}}) = \max\left(0, \eta_{i+1/2}^{\kappa}(\boldsymbol{\xi}_{\mathbf{p}}) - z_{i+1/2}^{\star}(\boldsymbol{\xi}_{\mathbf{p}})\right), \tag{B.8}$$

$$q_{i+1/2,k}^{\kappa,\star} = \sum_{r\in K}\sum_{s\in K} h_{i+1/2,r}^{\kappa,\star} u_{i+1/2,s}^{\kappa} \left\langle \Phi_r \Phi_s \Phi_k \right\rangle\ . \tag{B.9}$$

The numerical flux $\widetilde{\mathbf{F}}_{i+1/2}^{n}$ at interface $i+1/2$ is then calculated as $\widetilde{\mathbf{F}}_{i+1/2}^{n} = \widetilde{\mathbf{F}}(\mathbf{U}_{i+1/2}^{-,\star}, \mathbf{U}_{i+1/2}^{+,\star})$ where $\mathbf{U}_{i+1/2}^{\kappa,\star} = \left[h_{i+1/2}^{\kappa,\star}, q_{i+1/2}^{\kappa,\star}\right]^{\mathsf{T}}$. To ensure well-balancing where one cell is wet and its neighbouring cell is dry, another modification is made to the bed elevation such that $z_{i+1/2}^{\kappa,\dagger}$ is calculated as

$$z_{i+1/2,k}^{\kappa,\dagger} = z_{i+1/2,k}^{\star} - \Delta_{i+1/2,k}^{\kappa}\,, \tag{B.10}$$

where $\Delta_{i+1/2,k}^{\kappa}$ is calculated by quadrature at points $\boldsymbol{\xi}_{\mathbf{p}}$ such that

$$\Delta_{i+1/2}^{\kappa}(\boldsymbol{\xi}_{\mathbf{p}}) = \max\left(0, -\left[\eta_{i+1/2}^{\kappa}(\boldsymbol{\xi}_{\mathbf{p}}) - z_{i+1/2}^{\star}(\boldsymbol{\xi}_{\mathbf{p}})\right]\right), \tag{B.11}$$

which ensures that the bed elevation $z_{i+1/2}^{\kappa,\dagger}$ is not higher than the water surface elevation $\eta_{i+1/2}^{\kappa}$ (Liang and Marche, 2009).

Appendix C. Instructions for running the model codes

Python 3 software is available for download from Zenodo (Shaw et al., 2020a) which includes a 1D hydrodynamic model that can be configured as an intrusive or nonintrusive stochastic model, and preconfigured test cases as presented in section 4. First ensure that Python 3, NumPy and SciPy are installed. Then, install the stochastic Galerkin library and the hydrodynamic models:

```
pip3 install --user --editable pysg
pip3 install --user --editable pysgswe
```

To run the intrusive model:

```
pysgswe-intrusive <outputDir> <testCase>
  <basis> --max-basis <integer>
```

where `<testCase>` is either `criticalSteadyState`, `lakeAtRest`, `flumeFrictionTopography` or `tsengTranscritical`, `<basis>` is either `haar` or `hermite`, and the `--max-basis` value is the maximum Haar wavelet refinement level or Hermite polynomial order, according to the choice of basis. For test cases involving multiple sources of uncertainty, the `--basis-dimensions` flag must also be included. A tensor product basis is used unless `--truncate-basis` is specified. On running the model, several text files are written to the specified `<outputDir>` which include:

`statistics.initial.dat` Initial conditions with mean and standard deviation of topography, water depth, discharge and free-surface elevation

`statistics.end.dat` The same variables corresponding to the end of the simulation

`quadrature-point-solutions.dat` Values of topography, water depth, discharge and free-surface elevation at the quadrature points in the stochastic domain

Each file has one line per element with an explanatory header row prefixed by `#`. Additional data can be obtained with optional command-line flags: use `pysgswe-intrusive --help` for more information.

Running the nonintrusive model follows a similar procedure:

```
pysgswe-nonintrusive <outputDir> <testCase>
  --max-level <integer>
```

where `--max-level` specifies the maximum refinement level. The nonintrusive model can only be used with a Haar wavelet basis. Other command line options are the same as for the intrusive model.

References

Abgrall, R., Congedo, P.M., Geraci, G., 2017. Towards a unified multiresolution scheme for treating discontinuities in differential equations with uncertainties. Mathematics and Computers in Simulation 139, 1–22. doi:10.1016/j.matcom.2016.02.002.

Abgrall, R., Mishra, S., 2017. Uncertainty quantification for hyperbolic systems of conservation laws, in: Handbook of Numerical Analysis. Elsevier. volume 18, pp. 507–544. doi:10.1016/bs.hna.2016.11.003.

Bäck, J., Nobile, F., Tamellini, L., Tempone, R., 2011. Stochastic spectral Galerkin and collocation methods for PDEs with random coefficients: a numerical comparison, in: Spectral and high order methods for partial differential equations. Springer, pp. 43–62. doi:10.1007/978-3-642-15337-2_3.

Bates, P.D., Pappenberger, F., Romanowicz, R.J., 2014. Uncertainty in flood inundation modelling, in: Applied uncertainty analysis for flood risk management. World Scientific, pp. 232–269. doi:10.1142/9781848162716_0010.

Beven, K., 2005. On the concept of model structural error. Water Science and Technology 52, 167–175. doi:10.2166/wst.2005.0165.

Blatman, G., Sudret, B., 2011. Adaptive sparse polynomial chaos expansion based on *least angle regression*. Journal of Computational Physics 230, 2345–2367. doi:10.1016/j.jcp.2010.12.021.

Brodie, I.M., 2013. Rational Monte Carlo method for flood frequency analysis in urban catchments. Journal of Hydrology 486, 306–314. doi:10.1016/j.jhydrol.2013.01.039.

Caviedes-Voullième, D., Kesserwani, G., 2015. Benchmarking a multiresolution discontinuous Galerkin shallow water model: Implications for computational hydraulics. Advances in Water Resources 86, 14–31. doi:10.1016/j.advwatres.2015.09.016.

Cheng, M., Narayan, A., Qin, Y., Wang, P., Zhong, X., Zhu, X., 2019. An efficient solver for cumulative density function-based solutions of uncertain kinematic wave models. Journal of Computational Physics 382, 138–151. doi:10.1016/j.jcp.2019.01.008.

Debusschere, B.J., Najm, H.N., Pébay, P.P., Knio, O.M., Ghanem, R.G., Le Maître, O.P., 2004. Numerical challenges in the use of polynomial chaos representations for stochastic processes. SIAM Journal on Scientific Computing 26, 698–719. doi:10.1137/S1064827503427741.

Di Baldassarre, G., Schumann, G., Bates, P.D., Freer, J.E., Beven, K.J., 2010. Flood-plain mapping: a critical discussion of deterministic and probabilistic approaches. Hydrological Sciences Journal 55, 364–376. doi:10.1080/02626661003683389.

Dimitriadis, P., Tegos, A., Oikonomou, A., Pagana, V., Koukouvinos, A., Mamassis, N., Koutsoyiannis, D., Efstratiadis, A., 2016. Comparative evaluation of 1D and quasi-2D hydraulic models based on benchmark and real-world applications for uncertainty assessment in flood mapping. Journal of Hydrology 534, 478–492. doi:10.1016/j.jhydrol.2016.01.020.

El Moçayd, N., Ricci, S., Goutal, N., Rochoux, M.C., Boyaval, S., Goeury, C., Lucor, D., Thual, O., 2018. Polynomial surrogates for open-channel flows in random steady state. Environmental Modeling & Assessment 23, 309–331. doi:10.1007/s10666-017-9582-2.

Elman, H.C., Miller, C.W., Phipps, E.T., Tuminaro, R.S., 2011. Assessment of collocation and Galerkin approaches to linear diffusion equations with random data. International Journal for Uncertainty Quantification 1, 19–33. doi:10.1615/Int.J.UncertaintyQuantification.v1.i1.20.

Ge, L., Cheung, K.F., 2011. Spectral sampling method for uncertainty propagation in long-wave runup modeling. Journal of Hydraulic Engineering 137, 277–288. doi:10.1061/(ASCE)HY.1943-7900.0000301.

Ge, L., Cheung, K.F., Kobayashi, M.H., 2008. Stochastic solution for uncertainty propagation in nonlinear shallow-water equations. Journal of Hydraulic Engineering 134, 1732–1743. doi:10.1061/(ASCE)0733-9429(2008)134:12(1732).

Hiver, J., 2000. Adverse-slope and slope (bump), in: Concerted Action on Dam Break Modelling: Objectives, Project Report, Test Cases, Meeting Proceedings, Civil Engineering Department, Hydraulic Division, Universitè Catholique de Louvain.

Jung, Y., Merwade, V., 2011. Uncertainty quantification in flood inundation mapping using generalized likelihood uncertainty estimate and sensitivity analysis. Journal of Hydrologic Engineering 17, 507–520. doi:10.1061/(ASCE)HE.1943-5584.0000476.

Kesserwani, G., 2013. Topography discretization techniques for Godunov-type shallow water numerical models: a comparative study. Journal of Hydraulic Research 51, 351–367. doi:10.1080/00221686.2013.796574.

Kesserwani, G., Ayog, J.L., Bau, D., 2018. Discontinuous Galerkin formulation for 2D hydrodynamic modelling: Trade-offs between theoretical complexity and practical convenience. Computer Methods in Applied Mechanics and Engineering 342, 710–741. doi:10.1016/j.cma.2018.08.003.

Kesserwani, G., Shaw, J., Sharifian, M.K., Bau, D., Keylock, C., Bates, P.D., Ryan, J.K., 2019. (Multi)wavelets increase both accuracy and efficiency of standard Godunov-type hydrodynamic models. Advances in Water Resources 129, 31–55. doi:10.1016/j.advwatres.2019.04.019.

Kim, B., Sanders, B.F., 2016. Dam-break flood model uncertainty assessment: case study of extreme flooding with multiple dam failures in Gangneung, South Korea. Journal of Hydraulic Engineering 142, 05016002. doi:10.1061/(ASCE)HY.1943-7900.0001097.

Le Maître, O.P., Knio, O.M., Najm, H.N., Ghanem, R.G., 2004a. Uncertainty propagation using Wiener–Haar expansions. Journal of Computational Physics 197, 28–57. doi:10.1016/j.jcp.2003.11.033.

Le Maître, O.P., Nahm, H.N., Ghanem, R.G., Knio, O.M., 2004b. Multi-resolution analysis of Wiener-type uncertainty propagation schemes. Journal of Computational Physics 197, 502–531. doi:10.1016/j.jcp.2003.12.020.

Liang, Q., Marche, F., 2009. Numerical resolution of well-balanced shallow water equations with complex source terms. Advances in Water Resources 32, 873–884. doi:10.1016/j.advwatres.2009.02.010.

Mao, J., Zhao, L., Bai, X., Guo, B., Liu, Z., Li, T., 2016. A novel well-balanced scheme for modeling of dam break flow in drying-wetting areas. Computers & Fluids 136, 324–330. doi:10.1016/j.compfluid.2016.06.022.

Mishra, S., Schwab, C., Sukys, J., 2012. Multilevel Monte Carlo finite volume methods for shallow water equations with uncertain topography in multi-dimensions. SIAM Journal on Scientific Computing 34, B761–B784. doi:10.1137/110857295.

Murillo, J., Navas-Montilla, A., 2016. A comprehensive explanation and exercise of the source terms in hyperbolic systems using Roe type solutions. application to the 1D-2D shallow water equations. Advances in Water Resources 98, 70–96. doi:10.1016/j.advwatres.2016.10.019.

Neal, J., Keef, C., Bates, P., Beven, K., Leedal, D., 2013. Probabilistic flood risk mapping including spatial dependence. Hydrological Processes 27, 1349–1363. doi:10.1002/hyp.9572.

Pettersson, P., Iaccarino, G., Nordström, J., 2014. A stochastic Galerkin method for the Euler equations with Roe variable transformation. Journal of Computational Physics 257, 481–500. doi:10.1016/j.jcp.2013.10.011.

Pettersson, P., Tchelepi, H.A., 2016. Stochastic Galerkin framework with locally reduced bases for nonlinear two-phase transport in heterogeneous formations. Computer Methods in Applied Mechanics and Engineering 310, 367–387. doi:10.1016/j.cma.2016.07.013.

Roe, P.L., Pike, J., 1985. Efficient construction and utilisation of approximate Riemann solutions, in: Proc. of the 6th Int'l Symposium on Computing Methods in Applied Sciences and Engineering, VI, North-Holland Publishing Co., Amsterdam, The Netherlands. pp. 499–518.

Sharifian, M.K., Kesserwani, G., Hassanzadeh, Y., 2018. A discontinuous Galerkin approach for conservative modeling of fully nonlinear and weakly dispersive wave transformations. Ocean Modelling 125, 61–79. doi:10.1016/j.ocemod.2018.03.006.

Shaw, J., Kesserwani, G., 2020. Stochastic Galerkin finite volume shallow flow model: well-balanced treatment over uncertain topography. ASCE Journal of Hydraulic Engineering doi:10.1061/(ASCE)HY.1943-7900.0001705. accepted.

Shaw, J., Kesserwani, G., Pettersson, P., 2020a. Python 3 wavelet-based probabilistic hydrodynamic model with wetting-and-drying and friction under multiple uncertainties. URL: https://doi.org/10.5281/zenodo.3251990, doi:10.5281/zenodo.3251990.

Shaw, J., Kesserwani, G., Pettersson, P., 2020b. Stochastic hydrodynamic solution data with multiple uncertainties. URL: https://doi.org/10.5281/zenodo.3251720, doi:10.5281/zenodo.3251720.

Son, J., Du, Y., 2020. Comparison of intrusive and nonintrusive polynomial chaos expansion-based approaches for high dimensional parametric uncertainty quantification and propagation. Computers & Chemical Engineering 134. doi:10.1016/j.compchemeng.2019.106685.

Toro, E.F., Garcia-Navarro, P., 2007. Godunov-type methods for free-surface shallow flows: A review. Journal of Hydraulic Research 45, 736–751. doi:10.1080/00221686.2007.9521812.

Tryoen, J., Le Maître, O.P., Ern, A., 2012. Adaptive anisotropic spectral stochastic methods for uncertain scalar conservation laws. SIAM Journal on Scientific Computing 34, A2459–A2481. doi:10.1137/120863927.

Tseng, M.H., 2004. Improved treatment of source terms in TVD scheme for shallow water equations. Advances in Water Resources 27, 617–629. doi:10.1016/j.advwatres.2004.02.023.

Wang, P., Tartakovsky, D.M., 2012. Uncertainty quantification in kinematic-wave models. Journal of Computational Physics 231, 7868–7880. doi:10.1016/j.jcp.2012.07.030.

Wang, Y., Hu, K., Ren, L., Lin, G., 2019. Optimal observations-based retrieval of topography in 2D shallow water equations using PC-EnKF. Journal of Computational Physics 382, 43–60. doi:10.1016/j.jcp.2019.01.004.

Xiu, D., 2009. Fast numerical methods for stochastic computations: a review. Communications in Computational Physics 5, 242–272.

Xiu, D., Hesthaven, J.S., 2005. High-order collocation methods for differential equations with random inputs. SIAM Journal on Scientific Computing 27, 1118–1139. doi:10.1137/040615201.

Xiu, D., Karniadakis, G.E., 2002. The Wiener–Askey polynomial chaos for stochastic differential equations. SIAM Journal on Scientific Computing 24, 619–644. doi:10.1137/S1064827501387826.